Combustion and Flame 276 (2025) 114115

Contents lists available at ScienceDirect

Combustion and Flame

journal homepage: www.sciencedirect.com/journal/combustion-and-flame

Two dimensional flame structure of oscillating burner-stabilized methane-air flames

Ningyi Li [a,*], Viatcheslav Bykov [a], Anastasia Moroshkina [b], Evgeniy Sereshchenko [b], Vladimir Gubernov [b]

[a] Institute of Technical Thermodynamics, Karlsruhe Institute of Technology, Engelbert-Arndold-Strasse 4, Karlsruhe 76131, Germany
[b] P.N. Lebedev Physical Institute of Russian Academy of Sciences, 53 Leninskii prosp., Moscow 119991, Russian Federation

ARTICLE INFO

Keywords:
Burner-stabilized flames
Thermal-diffusion instability
Pulsating combustion regime
CFD
Model validation

ABSTRACT

The highly transient relaxational diffusive-thermal oscillations of flat burner-stabilized flames can be very attractive to probe the performance of detailed reaction mechanisms in the regimes close to ignition/extinction. In such regimes, certain reaction zones can travel over distances of the order of 10 mm and this raises an important question if one dimensional numerical models can be accurate in describing them. The question of quantitative comparison of modeling and experiments becomes crucial to study, to understand these regimes and to utilize them for validation. In this work, we experimentally investigate relaxational oscillations of methane-air flames on a flat porous burner with a surrounding nitrogen co-flow and perform fully resolved 2D numerical simulations of the same burner configuration, using a detailed reaction mechanism and molecular diffusion model, buoyancy and radiation, alongside corresponding experiments. The focus is on the effect of the nitrogen co-flow on the flame oscillations, which can only be studied numerically in 2D simulations due to the mutual effect of the complex flow field and flame dynamics. The results of both numerical and experimental approaches are found to be in quantitative agreement. They show that there is an optimal co-flow velocity that removes the secondary diffusion flame and extinguishes the edge flame settled in the stagnation flow region. This optimal regime makes the flame flatter and closer to a one-dimensional configuration and this is a most favorable condition for validation of kinetic mechanisms. The detailed data from the simulations will guide the design of the next generation of the burner configurations to study the kinetics and dynamics of complex fuels required for a sustainable energy transition.

Novelty and Significance Statement

The novelty of this research lies in the synergy of these modeling, computations with experimental measurements, allowing both parametric studies of the oscillation regime and deeper insights into the flame structure. These results are significant because they allow to develop more accurate burner configurations for studying flames near extinction and ignition conditions, which will be an important task for more complex fuels from renewable sources required for a sustainable energy transition. Ultimately, our understanding of the interplay between chemistry and diffusion controlled combustion regimes under transient conditions can be approved and validation data for e.g. chemical reaction mechanisms can be generated. The latter becomes extremely important since efficiency and pollutant mitigation issues require lean and chemistry controlled combustion processes used in the combustion facilities. Thus understanding, optimization and control of such regimes has become a crucial point for further development of the sustainable combustion.

1. Introduction

Flat porous burners are often used to investigate the structure of laminar flames and measure fundamental flame properties [1–7]. The advantage of this configuration is that it allows to form a flat reaction front with almost one-dimensional gas flow [6], which makes it possible to directly compare the experimental data with the predictions of one-dimensional numerical simulations with detailed reaction mechanisms [8–10], omitting the calculation of gas dynamics. Such a comparison can thus be employed to verify flame kinetics [7,11,12].

The general behavior of steady-state burner-stabilized flames is rather well understood and studied by now. The flames have been

* Corresponding author.
E-mail address: ningyi.li@partner.kit.edu (N. Li).

https://doi.org/10.1016/j.combustflame.2025.114115
Received 27 September 2024; Received in revised form 7 March 2025; Accepted 7 March 2025
Available online 23 March 2025

investigated experimentally [1,13–15], asymptotically [16–19] and numerically with one-step [19,20], reduced [21], and detailed models [15,22,23]. They exhibit a U-shaped response curve in terms of the dependence of the flame height above the burner on mass flow rate or flame temperature. The flames are blown off as the mass flow rate approaches the corresponding value from the freely propagating flame. In this case, the flame height is predicted to increase infinitely by the one-dimensional models, while in experiments the flame surfaces become corrugated and the luminous surface of the combustion front lifts off from the burner surface [15]. As the mass flow rate is decreased, the flame height passes through a minimum and then starts to depart from the burner surface. It should be noted that the flame temperature is a monotonic function of the mass flow rate and thus two flame temperatures can be observed for the same flame height [1,13,14]. It is also known that as the mass flow rate or flame temperature is decreased, diffusive-thermal oscillations can occur before or after the minimum stand-off condition is attained.

These pulsations are experimentally detected and investigated in [15,24–26] for the case of burner-stabilized methane-air flames. In particular, it is proposed to use the measured and numerically calculated characteristics of the diffusive-thermal oscillations in order to verify detailed reaction mechanisms for methane and other hydrocarbon fuels. In [22,23,27] we numerically analyzed critical conditions for the onset of the diffusive-thermal oscillations and the frequency of pulsations for the burner stabilized hydrogen-air flames by using various detailed reaction mechanisms. It was demonstrated that these characteristics of pulsating combustion fronts are very sensitive to the choice of the specific reaction mechanism and such behavior is more pronounced for the elevated pressure. In [15,24,25,28] the same parameters of the diffusive-thermal oscillations are investigated both numerically and experimentally for the case of the methane-air and methane-hydrogen-air burner stabilized flames. It is found that the predictions of the various detailed reaction mechanisms are scattered so that the uncertainty of the experimental measurements is smaller than the difference between the numerical data. The sensitivity analysis allowed us to reveal the key elementary reactions mostly responsible for the observed disagreement between the numerical and experimental results. In [26], the dynamics of flame oscillations are shown to be quite complex as we move in the plane of parameters away from the critical stability boundary for the onset of diffusive-thermal pulsations. In this case, inflow velocity is decreased to attain the pulsating solution with distinguished amplitudes of periodic flame front oscillations. In such regimes of relaxational oscillations, the flame front moves sufficiently away from the surface of the burner. Therefore, surrounding flow might further influence the complex flame structure and the question raised from [6] “How flat is the flame?” becomes very important.

In this work, we study the influence of a nitrogen co-flow on the oscillation characteristics of a burner-stabilized methane flame. For this, both experimental measurements and fully resolved detailed simulations are presented for the case corresponding to relaxational regime of flame pulsations.

2. Experimental setup

The scheme of the experimental setup is shown in Fig. 1. The main unit of the setup is the burner, the central part of which is a porous cylinder through which the methane-air mixture is supplied. The porous structure of the cylinder is an array of channels with a diameter of 0.2 mm and a distance between the centers of the channels of 0.4 mm. The central part of the burner is surrounded by a porous channel of 4 mm width for supplying a nitrogen co-flow, blocking the penetration of the surrounding air to the flame. The geometry of the burner is further described in Fig. 2(a). The burner is thermally stabilized by a circulation thermostat (LOIP LT-205a). The standard temperature (20 °C) of the burner and normal pressure are used for the measurements. Methane, nitrogen and air are supplied through mass

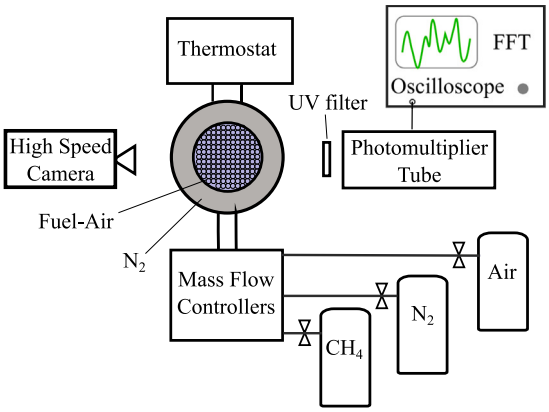

Fig. 1. Experimental setup.

flow controllers (Bronkhorst EL-FLOW Prestige). The investigation was focused on the dynamics of the flame and radical OH^* pulsations at mass flow rate of the mixture $M = 0.1$ kg/(m^2 s) and equivalence ratio $\phi = 1.15$ for different mass flow rates of nitrogen (m_{N_2}) in the range from 0 to 0.224 kg/(m^2 s). These conditions correspond to a highly relaxational regime of flame oscillations, which is chosen to represent such well developed pulsations as it is discussed below. Visual recording of the flame is implemented with a high speed camera (Evercam 2000-8-C). To analyze the chemiluminescence signal, a photomultiplier tube (Hamamatsu R1527) is used. An UV band-pass filter (Edmund Optics, center wavelength of 313 nm and full width at half maximum of 10 nm) ensures that only chemiluminescence from OH^* is transmitted. It almost perfectly covers the strong chemiluminescence emission lines of the OH^* (0,0) and (1,1) transition bands and also this spectral ranges does not contain the strong emission lines of other reaction species, which may interfere the OH^* chemiluminescence signal (see more details in [24]). The signal from the photomultiplier tube is recorded and processed by the digital oscilloscope (Tektronix MSO64 6-BW-2500), which allows to determine the frequency of pulsations.

3. Numerical setup

The flame configuration used in the computations follows the experimental set-up described above. The main methane-air jet with equivalence ratio of 1.15 is injected from an inner tube into a co-flowing pure nitrogen stream provided by an outer tube. The tubes through which the methane-air flow as well as the nitrogen flow are concentric with radii $R_I = 7.48$ mm and $R_O = 12.06$ mm, respectively (see Fig. 2(a)). The wall thickness of the two tubes is 1.61 mm. The outer zone is treated as an open air boundary condition, therefore, we consider the ambient air entrainment by the coflow. The two gases come into contact at the outlets of the inner and outer tubes. The flame establishes close the inner tube’s exit plane and remains confined, being separated by the co-flow from the surrounding. The black dashed line in Fig. 2(b) shows the computational domain. The computational domain is two-dimensional and axisymmetric, with dimensions $R_{MAX} = 22.44$ mm in radial direction (y-direction) and $L = 22.44$ cm in axial direction (x-direction). The axial length was selected based on preliminary studies that confirmed mesh independence at this length. The green rectangles show the locations of the wall between the two tubes, where no-slip boundary conditions are imposed.

In order to reduce the number of grid points and better resolve the flame structure, a reaction zone with a locally refined, uniform mesh is defined. The mesh size is uniformly distributed within this reaction zone, characterized by dimensions $\Delta x = 0.025$ mm and $\Delta y = 0.025$ mm. The thermal flame thickness of the 1D unstretched flame without oscillation (equivalence ratio 1.15) is 0.56 mm, which means there are

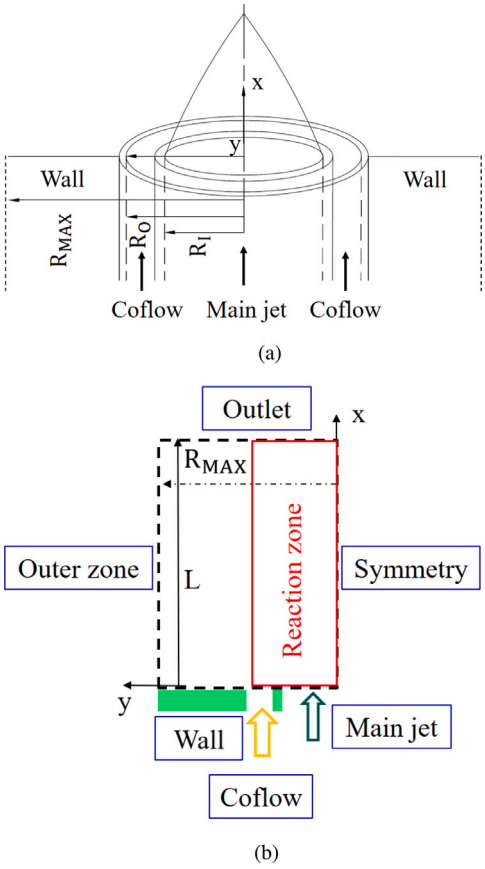

Fig. 2. Schematic illustration of the flame configuration (a) and the computational domain (b). (For interpretation of the references to color in this figure legend, the reader is referred to the web version of this article.)

approximately 22 grid points to resolve the flame front. Moreover, the grid resolution is also verified through 1D flame calculations, as shown in Fig. 3, which proved that the mesh size 0.025 mm is enough to resolve the thermal flame thickness.

Beyond this reaction domain, the mesh size increases proportionally with a grading ratio of 5 in the y direction. The streams from the inner and outer pipes are set to 293 K and the ambient air pressure is set to 1 bar. The mass fractions of the composition at the main jet are as follows: CH_4 (0.0629), N_2 (0.7188), and O_2 (0.2183). The mass fractions of nitrogen and oxygen in air are 0.768 and 0.232, respectively. The mass flow rate of the main jet (M) is 0.1 kg/(m^2 s), while the values for the co-flow (m_{N_2}) are 0, 0.037 and 0.094 kg/(m^2 s). The outer zone is treated as an open air boundary condition, and the outlet is also set to 1 bar, while other conditions of the outlet and outer zone are defined as zero gradient. To simulate the setup as an axisymmetric case in 2D cylindrical coordinates, an axisymmetric symmetry boundary condition (depicted as "symmetry" in Fig. 2(b)) is applied [29].

The simulations are performed with the finite volume code EBIdnsFoam [30,31], which uses OpenFOAM [32] to solve the fully compressible Navier–Stokes equations, together with the balance equations for energy and species masses. The code is coupled to Cantera [10], which provides detailed transport coefficients for each species based on the Hirschfelder and Curtiss approximation [33]. Additionally, Soret diffusion is considered [34]. Chemical reaction rates are computed from finite rate chemistry based on the GRI 3.0 mechanism [35] and an optically thin radiation model with four radiating species (H_2O, CO, CO_2 and CH_4) is taken into account in the calculation, the details of which are found in [36,37]. Buoyancy is included in the simulations. All spatial derivatives are discretized with fourth-order interpolation schemes and a second-order implicit time stepping is used with an adaptive time step ensuring CFL < 0.2.

To correctly model the flame near the burner plate, a new Robin-type boundary condition was implemented in the framework of OpenFOAM to ensure nonzero flux $\vec{j}_k$ for each species k at the boundary [38]. The diffusive flux of the species is formulated as

$$\vec{j}_k = -\rho D_k \nabla Y_k - Y_k \rho D_k \frac{\nabla \bar{M}}{\bar{M}} - D_k^T \frac{\nabla T}{T}, \tag{1}$$

where ρ is the density, D_k the diffusion coefficient of species k, $\bar{M}$ the mean molar mass of the gas and D_k^T the Soret diffusion coefficient of the species. Accordingly, the species mass fraction at the boundary cell face b is computed from

$$\dot{m}_0 \left(Y_{k,b} - Y_{k,0}\right) \vec{n}_b = -\vec{j}_k \cdot \vec{n}_b \tag{2}$$

where $Y_{k,b}$ is the species mass fraction at the boundary face, $\dot{m}_0$ is the reference mass flow rate, $Y_{k,0}$ the reference species mass fraction based on the prescribed equivalence ratio, $\vec{n}_b$ is the boundary face normal vector.

The boundary condition Eq. (2) ensures that the total flux (i.e. convection and diffusion) equals the reference mass flux $\dot{m}_{k,0} = \dot{m}_0 Y_{k,0}$. This is required when the flame comes near to the inlet and would cause an addition diffusive flux. Therefore, $\vec{j}_k$ is not zero but adjusted to achieve a total mass flux of $\dot{m}_{k,0}$. Likewise, the velocity at the inlet of the main jet is computed ensuring constant mass flux as

$$\vec{u}_b = \vec{n}_b \frac{\dot{m}_0}{\rho_b}. \tag{3}$$

4. Results and discussion

The experimental and numerical studies in [25] and the current study (see Fig. 4) shows that the stability boundary $M_{cr}(\phi)$ for the onset of oscillations appears as a bell-shaped curve in the plane of parameters ϕ vs. M. The lean side of the stability boundary $M(\phi)$ can be traced up to the values of the equivalence ratio $\phi \approx 0.95$ while the rich slope up to $\phi \approx 1.6$ at which the mass flow rate becomes very small $M \leq 0.05$ kg/m^{2}s and the flame very weak. The peak of the $M(\phi)$ dependence is reached at $\phi \approx 1.15$ corresponding to $M \approx 0.22$ kg/(m^2 s). This value of the equivalence ratio is chosen in the current investigations since it allows to change the mass flow rate in a wider range of values and to study various regimes of flame oscillations especially in the case of relaxational oscillations when the parameters are chosen sufficiently away from the critical ones corresponding to the onset of pulsations.

In [26], it is found that as M is decreased below the critical value M_{cr} for the emergence of the instability, the flame oscillations become more and more relaxational. There occur stages of fast reactivity replaced by relatively long periods of depression. At certain values of M, the flame pulsation dynamics appear similar to the FREI regime [39]. The flame structure can even dynamically separate in space into high and low-temperature reaction zones with further reduction of M [26]. In such highly transient regimes, the location of the various reaction zones can depart significantly from the surface of the burner over distances of the order of 10 mm. In the current experimental study, as Fig. 4 demonstrates, we mainly focus on such a regime of pulsations and choose a mass flow rate of $M = 0.1$ kg/(m^2 s). The analysis of the system in such conditions is of special interest, since it allows us to put the flame close to the conditions of quenching and ignition, spread and separate various reaction zone and study them [26], which is not possible in normal propagating flame conditions. In [25], it is reported that the nitrogen co-flow can impact the structure of the burner-stabilized flames. In the configuration without co-flow, a secondary diffusion combustion front can form in the case of $\phi > 1$, which appears as a conical Bunsen-like flame on top of the main planar premixed flame. It is also discussed [25] that characteristics of diffusive-thermal oscillations can be affected by the presence of this diffusion flame.

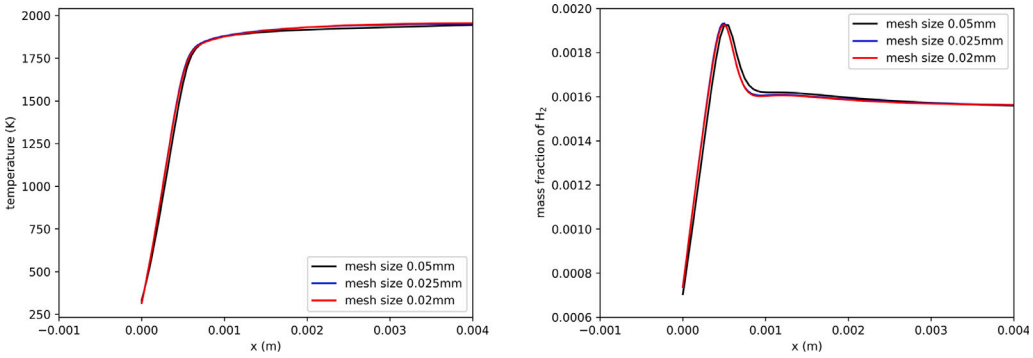

Fig. 3. Validation of mesh dependence in 1D flame (temperature (a) and mass fraction of H_2 (b)).

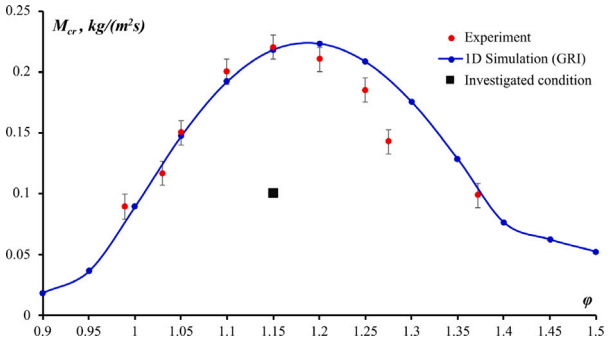

Fig. 4. Dependencies of M_{cr} on φ obtained experimentally (red markers) and numerically (blue markers) within the GRI mechanism [35] using INSFLA [9]. Black square indicates the parameters under which this study was conducted. (For interpretation of the references to color in this figure legend, the reader is referred to the web version of this article.)

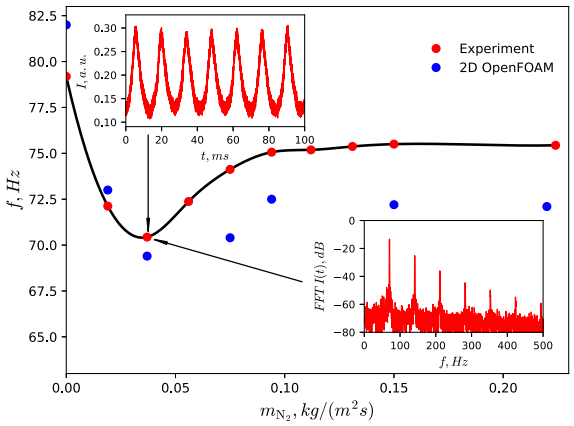

Fig. 5. Dependence of oscillation frequency on nitrogen flow rate. (For interpretation of the references to color in this figure legend, the reader is referred to the web version of this article.)

The nitrogen co-flow is shown to effectively suppress the secondary diffusion flame. However, in [25], small oscillations emerging for operating conditions close to the neutral stability boundary are mainly studied, while it is not clear how strongly the co-flow influences the characteristics of relaxational pulsations. Therefore, our studies are focused on these conditions.

4.1. Experimental results

The onset, dynamics and characteristics of flame oscillations are experimentally analyzed by recording and processing the signal of OH* chemiluminescence according to the scheme in Fig. 1. The typical oscillogram of the chemiluminescence signal, $I(t)$, is shown in Fig. 5 in the top subfigure for $\phi = 1.15$ and $M = 0.1$ kg/(m^2 s). Fast Fourier transformation of $I(t)$ was constructed online by using the digital oscilloscope, which allowed us to determine its spectral characteristics. The Fourier spectrum of $I(t)$ is presented in the right-bottom sub-figure of Fig. 5 and it corresponds to the signal plotted in the top sub-figure. The structure of the spectrum clearly demonstrates the periodic nature of the oscillations. It contains several well-resolved equidistant lines that are multiples of the flame oscillation frequency, f, thus allowing us to directly measure it.

Next, we investigate how the co-flow intensity influences the characteristics of pulsations by measuring f at various values of mass flow rate of nitrogen, m_{N_2}. In Fig. 5, the dependence of the oscillation frequency determined as it is described above is plotted as a function of the mass flow rate of nitrogen for $\phi = 1.15$ and $M = 0.1$ kg/(m^2 s) with the red circles. There is a significant decay of f as m_{N_2} is slightly increased from zero. At $m_{N_2} = 0.037$ kg/(m^2 s) the frequency attains minimum and at $m_{N_2} = 0.094$ kg/(m^2 s) reaches saturation and tends to a constant value for larger m_{N_2}. It is noteworthy that at $m_{N_2} = 0.094$ kg/(m^2 s) the linear velocities of nitrogen and methane-air flows at the burner surface become equal. In some sense, the maximum 'shielding' effect of the co-flow is achieved at this stage and further increase of m_{N_2} does not alter the characteristics of the flame oscillations. A nontrivial behavior of f for $m_{N_2} < 0.1$ kg/(m^2 s) is related to a significant change of the flame structure, which is illustrated in Fig. 6, where the photographs of the flame are shown for various values of $m_{N_2} = 0$, 0.037, 0.075, and 0.094 kg/(m^2 s). The photographs are taken for the exposition time 0.25 s, thus they represent time averaged behavior of pulsating flames over many tens of periods. It is clearly seen that as m_{N_2} is increased from zero, the secondary diffusion flame elongates at the tip for $m_{N_2} = 0.037$ kg/(m^2 s) and lifts off at 0.075 kg/(m^2 s). For $m_{N_2} = 0.094$ kg/(m^2 s) the gap between the base of the diffusion flame and burner surface becomes large and the influence of it diminishes with further m_{N_2} increase.

The structure of the pulsating flame is also illustrated in Fig. 7 for $m_{N_2} = 0.037$ kg/(m^2 s), where the results of the high speed imaging are summarized. In the top figures, the flame photographs taken at the exposure time 0.5 ms are demonstrated for four time instances along one oscillation period. The small deviation of the leading part of the flame from the planar form is clearly observed. The dynamics and the structure of flame pulsations are also presented in the main part of Fig. 7, where flame luminosity is plotted as a function of the distance from the burner surface, h. The luminosity or intensity is defined from the flame photographs. Every point in the digital flame image is encoded as an integer number from 0 to 256. The intensity

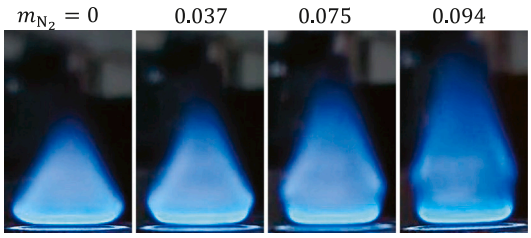

Fig. 6. Flame photos at different nitrogen mass flow rates.

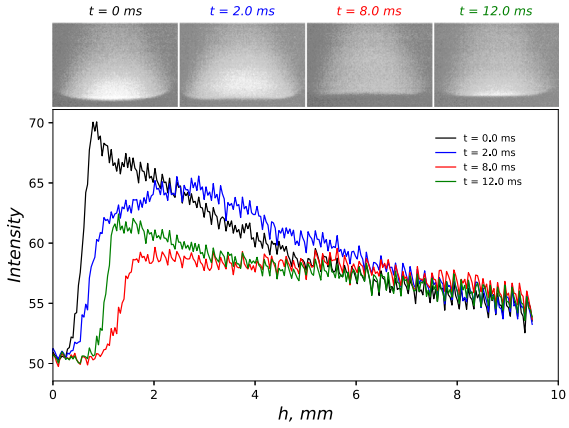

Fig. 7. Structure of the pulsating flame for m_{N_2} = 0.037 kg/(m^2 s). The top figure show the results of the high speed imaging, while the bottom figure represents the dependence of flame luminosity along the burner center line as a function of flame height.

function at each horizontal line of pixels is determined as an averaged value over 50 pixels located symmetrically with respect to the vertical center line of the image. The initial time, t = 0.0 ms, corresponds to the stage of the maximum reactivity at which the peak luminosity and the smallest stand-off distance are achieved. This intensifies the heat losses to the burner surface and at the subsequent time instances the flame luminosity starts to decay and the reaction front drifts downstream until the stage of minimum reactivity is reached at t = 8.0 ms. The increase of the flame height results in the reduction of heat losses to the burner and as reactivity increases, the peak luminosity grows and the flame shifts upstream to the burner at t = 12 ms. This process is periodically repeated in time.

4.2. Computational results

In the modeling several phenomena need to be taken into consideration. In 1D formulation the authors have shown that differential and thermal diffusion, mixed boundary conditions are necessary to come to quantitative comparisons since the difference between different models and boundary conditions implemented may be significant. In the current study the effect of thermal radiation heat losses, co-flow and buoyancy is quantified and investigated additionally. The later two require to treat the burner stabilized flame in 2D spatial consideration.

The morphology of the oscillating burner stabilized flames can be characterized by the spatial distribution of the radical species [22,26]. As it is discussed in [26], the dynamics of the main radials involved in the chain-branching process such as O, OH, H is correlated and their distribution with the distance from the burner surface remain a single peak function, unless the oscillations are turned into very strong relaxational mode by reducing the mass flow rate to sufficiently small values. Since the latter regime is not a subject of the current investigation, the instant distribution of one of these radicals can be taken to characterize the location of the flame front. In the current

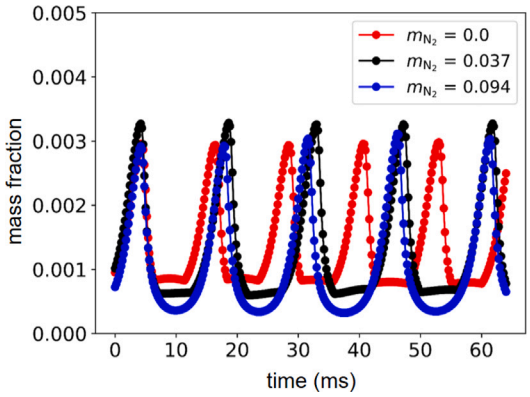

Fig. 8. Maximum of OH mass fractions along the center line during the last five periods.

work we use the distribution of OH radicals. One of the advantages of this choice is that OH concentration can be successfully measured by Laser induced fluorescence method. Thus the results of the current investigation can be compared to such experimental measurements in the future.

4.2.1. Co-flow of the inert gas

In order to proceed with the quantitative comparison between measurements and simulations, several nitrogen co-flow mass flow rates in the parameter space were taken for the same rich mixture composition (ϕ = 1.15, M = 0.1 kg/(m^2 s)) as in the experiment to study the secondary flame and its influence on pulsations and oscillating flame structure. To illustrate the convergence of the periodic solutions of the flame, the maximum of OH mass fractions along the center line during the last five periods is shown in Fig. 8. The figure shows that the solutions obtained are fully periodic, showing that the simulations were run until statistical convergence was achieved. The oscillations frequency (blue circles) obtained for each case with the numerical integration is shown in Fig. 5. The maximum of the frequency occurs at m_{N_2} = 0 kg/(m^2 s). As the co-flow mass flow rate increases to 0.037 kg/(m^2 s), the frequency rapidly decreases to its minimum value, aligning with the observed experimental results. Continuing to raise the mass flow rate to 0.094 kg/(m^2 s) results in a corresponding increase in the frequency, which again aligns with the experimental trends.

Figs. 9–11 show the OH mass fractions at different co-flow mass flow rates. The four sub-figures above the figures show contour plots of OH mass fraction at four different time steps. They are chosen at various stages in the flame dynamics associated with the growth of OH concentration (a), peak reactivity (b), decay of OH concentration (c) and depression (d). In Fig. 7 these stages of pulsating dynamics correspond to the moments of time t =12, 0, 2, and 8 ms, respectively. Since the frequency of oscillations in different regimes, shown in Figs. 9–11, 13 depends on the rate of co-flow of nitrogen, in each case these stages of dynamics are characterized by various time instants. The maximum of OH mass fractions along the center line is shown in the middle sub-figure (red line with points). The different colored lines represent the OH mass fractions along the center line at different time instances, corresponding to the time steps of the four sub-figures above. In Fig. 9, without the nitrogen co-flow, the results illustrate that an additional local maximum of the OH radical mass fraction located far from the burner surface is observed along the center line of the burner at a distance of about 8 mm from the surface. This signifies the presence of a secondary diffusion flame. The maximum of the OH mass fraction along the center line remains relatively constant for a portion of the period, as shown in Fig. 8. This phenomenon is attributed to the secondary diffusion flame that can clearly be seen in the contour plots of OH in upper figures.

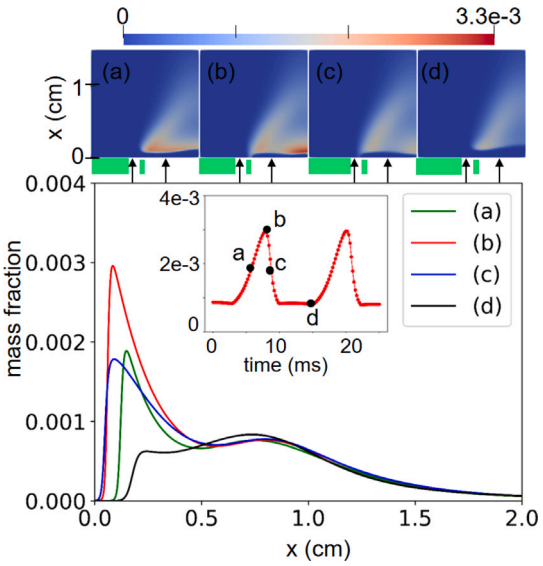

Fig. 9. OH mass fraction for mass flow rate m_{N_2} = 0 kg/(m^2 s); different colored lines represent the OH mass fraction along the center line at different time instances, (a) t = 5.8 ms, (b) t = 7.8 ms, (c) t = 8.8 ms, (d) t = 14.8 ms; the red line with points shows the maximum of OH mass fraction along the center line at the different times. (For interpretation of the references to color in this figure legend, the reader is referred to the web version of this article.)

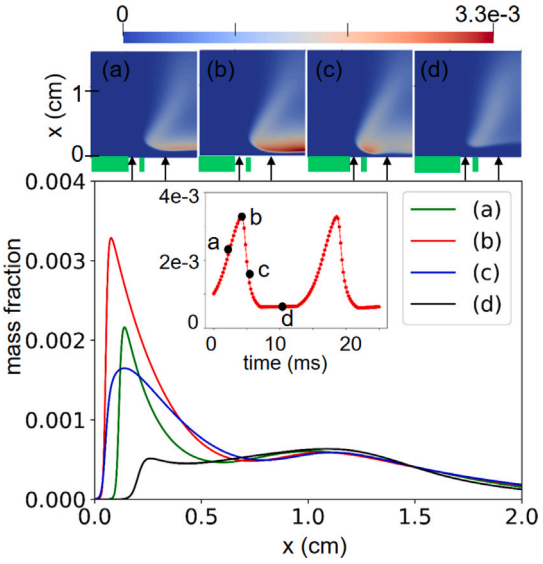

Fig. 10. OH mass fraction for mass flow rate m_{N_2} = 0.037 kg/(m^2 s); different colored lines represent the OH mass fraction along the center line at the different time instances, (a) t = 2.2 ms, (b) t = 4.2 ms, (c) t = 5.2 ms, (d) t = 11.2 ms; the red line with points shows the maximum of OH mass fraction along the center line at the different times. (For interpretation of the references to color in this figure legend, the reader is referred to the web version of this article.)

The mass fractions of OH for m_{N_2} = 0.037 kg/(m^2 s) is shown in Fig. 10. In comparison to Fig. 9, it is evident that, following the increase in mass flow rate, the secondary diffusion flame elongates prominently at the tip. The maximum value of the OH mass fraction along the center line remains constant for a specific interval of the period, which is similar to the results of m_{N_2} = 0 kg/(m^2 s) in Fig. 8. However, in contrast to Fig. 9, the OH mass fraction along the center line is smaller than that in Fig. 9 at the position of the secondary diffusion flame, but OH profile becomes broader and shifts to the right. This means that the secondary diffusion flame is suppressed by the nitrogen co-flow.

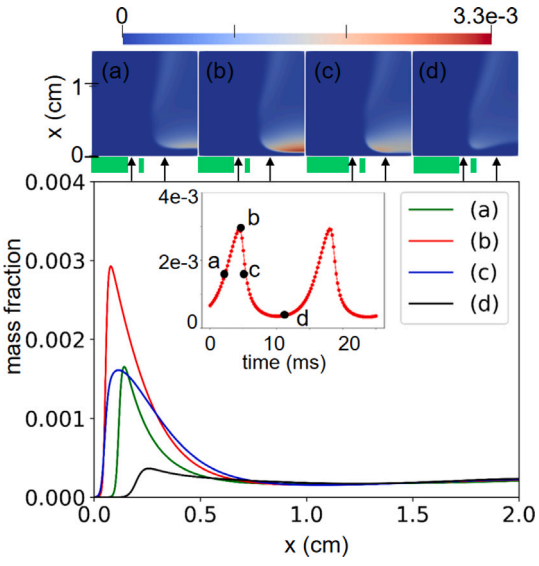

Fig. 11. OH mass fraction for mass flow rate m_{N_2} = 0.094 kg/(m^2 s); different colored lines represent the OH mass fraction along the center line at the different time steps, (a) t = 2.4 ms, (b) t = 4.4 ms, (c) t = 5.4 ms, (d) t = 11.4 ms; the red line with points shows the maximum of OH mass fraction along the center line at the different time steps. (For interpretation of the references to color in this figure legend, the reader is referred to the web version of this article.)

Fig. 11 indicates the OH mass fractions for m_{N_2} = 0.094 kg/(m^2 s). It is clearly shown that the second local maximum of OH is not present and the secondary diffusion flame is separated from the main flame due to the influence of the co-flowing nitrogen. Moreover, the absence of a consistent maximum OH value along the center line indicates that the second diffusion flame is further suppressed by the co-flowing nitrogen. We omit the discussion of the third case m_{N_2} = 0.075 kg/(m^2 s), since it is similar to the last one where the frequency "saturated" and no second maximum of OH is observed.

A significant change of flame morphology with the increase of co-flow mass flow rate can be observed in the 2D figures of OH mass fraction distribution in Figs. 9–11. The flame shows a well resolved edge flame structure at m_{N_2} = 0. There is a hot spot of OH near the end of the tube separating the methane-air and nitrogen flows. The diffusion and premixed flames branch out at an angle of around 45 ° (see Fig. 9(a)). The OH hot spot remains anchored to the surface of the wall in a stagnation flow during the whole oscillation period. The surface of the premixed flame bends and anchors between the surface of the burner and the diffusion flame. The OH hot spot disappears as the nitrogen flow rate is increased to m_{N_2} = 0.094 kg/(m^2 s) and the secondary diffusion flame is lifted from both the surface of the burner and the premixed combustion front, which appear uniform along the y-direction. The effect of the stagnation flow region can still be traced in Fig. 11(d), where some local increase of OH mass fraction is seen at the left-bottom corner of the reaction front. To summarize, it is seen that there is an optimal conditions that corresponds to the co-flow rate that removes the diffusion flame and it corresponds to the case, when the oscillation frequency begins to tend to a constant value. This is evidenced by both experiments and numerical calculations. Further increase of m_{N_2} does not affect the frequency, since the main source of the disturbance – the diffusion flame – is eliminated. The non-trivial dependence of the behavior of the oscillation frequency on the co-flow can be attributed to the entrainment of the outer air. The effect of ambient air entrainment is twofold: it provides oxygen for the secondary diffusion flame and imposes additional cooling. The first effect supports the combustion on the primary premixed flame, while the latter inhibits it. Thus, the increase of m_{N_2} switches two mechanisms one of which leads to the increase, while the other to the decrease of

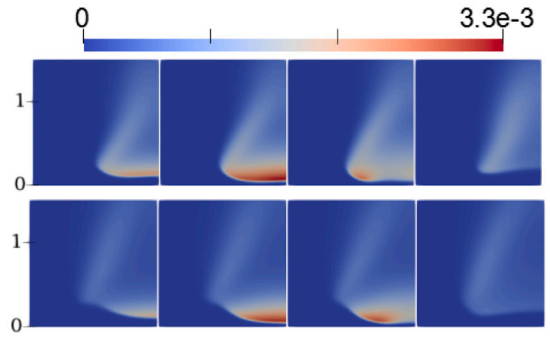

(a) Top/bottom snapshots: with/without buoyancy

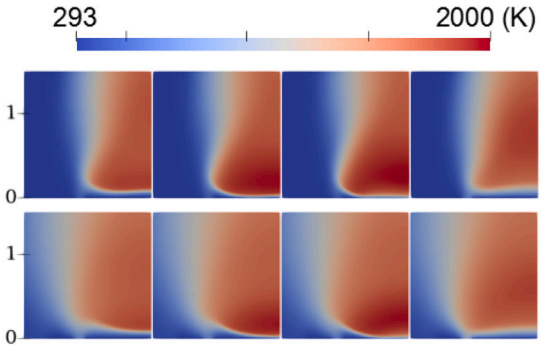

(b) Top/bottom snapshots: with/without buoyancy

Fig. 12. OH mass fraction (a) and temperature (b) with/without buoyancy for mass flow rate m_{N_2} = 0.037 kg/(m^2 s) at the different times.

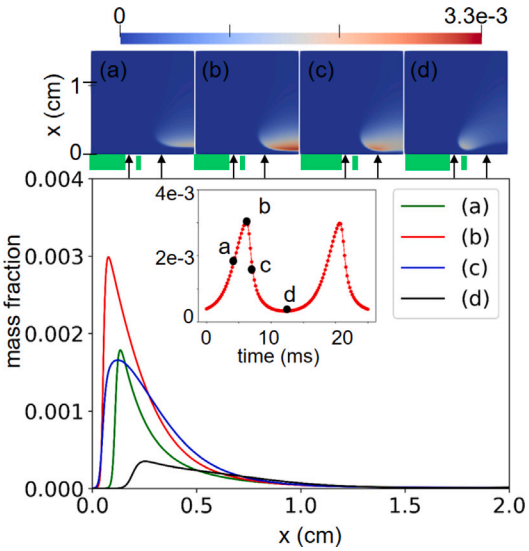

Fig. 13. OH mass fraction for mass flow rate m_{N_2} = 0.22 kg/(m^2 s); different colored lines represent the OH mass fraction along the center line at the different time instances, (a) t = 4.2 ms, (b) t = 6.2 ms, (c) t = 7.2 ms, (d) t = 12.2 ms; the red line with points shows the maximum of OH mass fraction along the center line at the different times. (For interpretation of the references to color in this figure legend, the reader is referred to the web version of this article.)

the frequency of pulsations, causing the nontrivial dependence of f on m_{N_2}. At $m_{N_2} > 0.094$ both effects disappear as the complete shielding effect is attained.

4.2.2. Buoyancy

The case of mass flow rate m_{N_2} = 0.037 kg/(m^2 s) is computed without buoyancy. Fig. 12 demonstrates the difference by snapshot of OH mass fraction (Fig. 12(a)) and temperature fields (Fig. 12(b)). Also the flame structure seen by OH is not perturbed much the main difference and influence is observed in cooling effect of the co-flow on flame seen by change of the temperature field near the separation between the main- and co-flow. This affects also the oscillation frequency. The oscillation frequency with or without buoyancy in this case is 69 Hz and 64 Hz, respectively. The experimental value is 70 Hz showing that by taking the effect into account the results with the buoyancy are closer to the experimental ones. Therefore, the effect of buoyancy is considered in all 2D calculations in this paper. The buoyancy effect enhances the convection between the surrounding air and the flame, which makes the oxidant enter the reaction zone faster to react with the fuel. This explains why the second diffusion flame is closer to the flame axis and the reaction zone is shorter, as shown in Fig. 12. The buoyancy increases the frequency of extinction-re-ignition because the convection allows more oxidant to enter the reaction zone, thereby shortening the re-ignition time, as shown in Fig. 14(b).

4.2.3. 1D versus 2D computations and discussion

In order to compare quantitatively the 1D and 2D computations and to make sure no 2D phenomena might have the influence on the flame structure the case of further increased mass co-flow rate m_{N_2} = 0.22 kg/(m^2 s) in Fig. 13, where the frequency is already reaches the plateau shown in Fig. 5, is considered. The secondary reaction zone is also cut-off by the co-flow of the inert gas similarly to Fig. 11, but now no traces of OH in the far field are observed. The secondary reaction zone is suppressed contrary to Figs. 9–10 and as profiles show no significant OH radical concentrations are observed beyond the close vicinity of the burner surface during the entire period of pulsating behavior.

Moreover, for this case of mass flow rate m_{N_2} = 0.22 kg/(m^2 s) the computation results of 1D and 2D are compared directly. Fig. 14 shows maxima of OH radical and location of OH maximum (the distance between the maxima and the burner exit) along the center line for one period of oscillations. The figure demonstrates very similar time history of maxima along the solution profile. One can see the slight overshoot of the maxima and slight shift in the position of maxima along the period, which is manifested as well in the frequency discrepancy.

Fig. 14 shows that the OH maximum occurs at 6 ms, and the flame front is very close to the burner surface, then it extinguishes and is pushed away from the surface. At 15 ms, it reignites again and moves towards the burner surface, and the cycle repeats. The reaction zone can travel over distances during this process, with the minimum and maximum being 0.68 mm and 2.73 mm in 1D and 0.70 mm and 3.02 mm in 2D computations, respectively, as shown in Fig. 14(b). The small difference in frequency between 1D (65 Hz) and 2D (69 Hz) is due to the buoyancy effect, as the buoyancy is higher in the 2D simulation.

Nevertheless, the flame front structure observed and investigated can be used to guide the design of the burner and co-flow such that the results will be close to 1D computations, which might be used to quickly access validity of 1D. The latter can be used to speed-up for parametric studies and for preliminary search for further interesting regimes.

5. Conclusions

In this work, we studied transient pulsating regimes of burner-stabilized flames. The case of slightly rich composition is taken as a representative example for detailed comparison of the flame dynamics and its structure. The inflow conditions were taken to correspond to the case when pulsations are well developed with representative amplitude of the flame form oscillations.

The question of quantitative comparison of experiments and computations was the focus of the study. The influence of the nitrogen co-flow onto the properties and structure of the pulsating flame front was

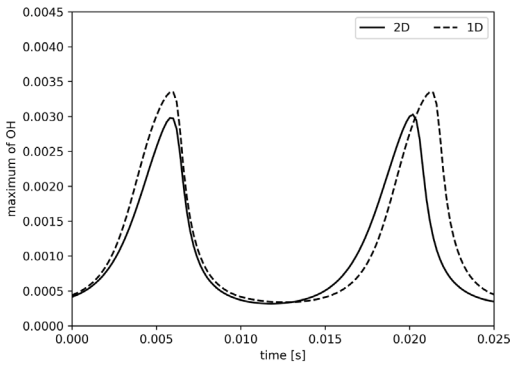

(a)

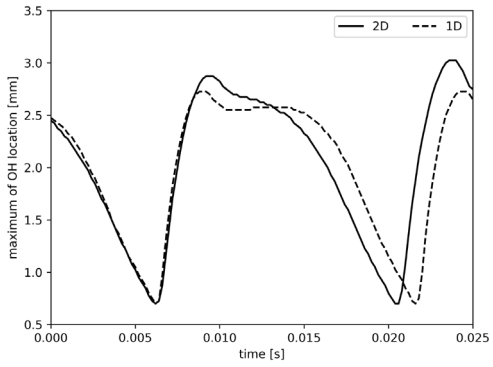

(b)

Fig. 14. Comparison of 1D and 2D maximum of OH mass fraction (a) and location of OH maximum (b) along the center-line with mass flow rate $m_{N_2} = 0.22$ kg/(m^2 s) over one period of pulsations.

addressed in detail. It has been confirmed here that for the quantitative comparison detailed diffusion, chemistry and radiation model need to be taken into account. Moreover, one should also consider the Robin (mixing) boundary conditions on the burner surface to model the flux into the porous burner matrix. Since the flame structure of the burner stabilized flame is inherently two-dimensional for a wider range of operating conditions, simulations of fully resolved complex flow field were conducted for the first time. Without these models and simulation approaches, quantitative comparison with the measurements is not possible.

Specifically, one can summarize the main results as following.

1. The nitrogen co-flow quantitatively influences the properties of the pulsating solution up to about 10 % in experiments and 15 % in computations;
2. Both experiments and computations agree and the difference (e.g. in frequency) is less then that observed for the different co-flow velocities;
3. An optimal co-flow velocity was found and this corresponds to the velocity that removes the diffusion flame and extinguishes the edge flame settled in the stagnation flow region;
4. Optimal regime makes the flame flatter and closer to one-dimensional, which is very important for speeding up parameter investigations and providing model validation;
5. The simulation results allow a detailed study of the flame structure in radial and axial direction, e.g. by providing resolved fields of OH mass fraction;
6. The information obtained from this work will guide the design of the next generation of the burner configurations to be designed and developed in future.

This information gives valuable directions for further improvement of the experimental setup to study combustion in regimes near flammability limits, which will be important for complex fuels produced from renewable sources to facilitate sustainable combustion. As a final outlook regarding the burner configuration, the wall thickness separating the flows needs to be decreased as much as possible to avoid the effects of flame anchoring near end surface.

CRediT authorship contribution statement

Ningyi Li: Writing – original draft, Validation, Formal analysis, Data curation. **Viatcheslav Bykov:** Writing – review & editing, Supervision, Methodology, Formal analysis. **Anastasia Moroshkina:** Writing – review & editing, Formal analysis, Data curation. **Evgeniy Sereshchenko:** Writing – original draft, Formal analysis. **Vladimir Gubernov:** Writing – review & editing, Supervision, Methodology, Formal analysis.

Declaration of competing interest

The authors declare that they have no known competing financial interests or personal relationships that could have appeared to influence the work reported in this paper.

Acknowledgment

We thank Dr. Thorsten Zirwes for useful discussion about the numerical implementation.

References

[1] D.B. Spalding, V.S. Yumlu, Experimental demonstration of the existence of two flame speeds, Combust. Flame 3 (1959) 553–556.
[2] J.P. Botha, D.B. Spalding, The laminar flame speed of propane/air mixtures with heat extraction from the flame, Proc. R. Soc. A: Math. Phys. Eng. Sci. 225 (1160) (1954) 71–96.
[3] L.P.H. De Goey, A. Van Maaren, R.M. Quax, Stabilization of adiabatic premixed laminar flames on a flat flame burner, Combust. Sci. Technol. 92 (1–3) (1993) 201–207.
[4] S. Prucker, W. Meier, W. Stricker, A flat flame burner as calibration source for combustion research: Temperatures and species concentrations of premixed H_2/air flames, Rev. Sci. Instrum. 65 (9) (1994) 2908–2911.
[5] G. Sutton, Andrew Levick, Gordon Edwards, Douglas Greenhalgh, A combustion temperature and species standard for the calibration of laser diagnostic techniques, Combust. Flame 147 (1–2) (2006) 39–48.
[6] Fr Migliorini, S. De Iuliis, F. Cignoli, G. Zizak, How "flat" is the rich premixed flame produced by your McKenna burner? Combust. Flame 153 (3) (2008) 384–393.
[7] D.A. Knyazkov, A.M. Dmitriev, T.A. Bolshova, V.M. Shvartsberg, A.G. Shmakov, O.P. Korobeinichev, Structure of premixed H_2/O_2/Ar flames at 1–5 atm studied by molecular beam mass spectrometry and numerical simulation, Proc. Combust. Inst. 36 (2017) 1233–1240.
[8] R.J. Kee, J.A. Miller, T.H. Jefferson, CHEMKIN: A General-Purpose, Problem-Independent, Transportable, FORTRAN Chemical Kinetics Code Package, Tech. Rep., (SAND80-8003) Sandia National Laboratories, 1980.
[9] U. Maas, J. Warnatz, Ignition processes in hydrogen-oxygen mixtures, Combust. Flame 74 (1) (1988) 53–69.
[10] D.G. Goodwin, R.L. Speth, H.K. Moffat, B.W. Weber, Cantera: an object-oriented software toolkit for chemical kinetics, thermodynamics, and transport processes, 2016, Version 2.2.1. https://www.cantera.org.
[11] Jacques Vandooren, Jiang Bian, Validation of H_2/O_2 reaction mechanisms by comparison with the experimental structure of a rich hydrogen-oxygen flame, Symp. (Int.) Combust. 23 (1991) 341–346.
[12] D.A. Knyazkov, Artëm M. Dmitriev, Oleg P. Korobeinichev, Ksenia N. Osipova, Gianmaria Pio, Andrey G. Shmakov, Ernesto Salzano, Structure of premixed flames of propylene oxide: Molecular beam mass spectrometric study and numerical simulation, Proc. Combust. Inst. 38 (2021) 2467–2475.
[13] W.E. Kaskan, The dependence of flame temperature on mass burning velocity, Symp. (Int.) Combust. 6 (1957) 134–143.
[14] C.R. Ferguson, J.C. Keck, Stand-off distances on a flat flame burner, Combust. Flame 34 (1979) 85–98.

[15] S. Nechipurenko, T. Miroshnichenko, N. Pestovskii, S. Tskhai, B. Kichatov, V.V. Gubernov, V. Bykov, U. Maas, Experimental observation of diffusive-thermal oscillations of burner stabilized methane-air flames, Combust. Flame 213 (2020) 202–210.
[16] Bernard J. Matkowsky, David O. Olagunju, Pulsations in a burner-stabilized premixed plane flame, SIAM J. Appl. Math. 40 (3) (1981) 551–562.
[17] G. Joulin, Flame oscillations induced by conductive losses to a flat burner, Combust. Flame 46 (1982) 271–281.
[18] J. Buckmaster, Stability of the porous plug burner flame, SIAM J. Appl. Math. 43 (6) (1983) 1335–1349.
[19] Vadim N. Kurdyumov, Moshe Matalon, The porous-plug burner: Flame stabilization, onset of oscillation, and restabilization, Combust. Flame 153 (1) (2008) 105–118.
[20] Vadim N. Kurdyumov, Mario Sánchez-Sanz, Influence of radiation losses on the stability of premixed flames on a porous-plug burner, Proc. Combust. Inst. 34 (2013) 989–996.
[21] Stephen B. Margolis, Bifurcation phenomena in burner-stabilized premixed flames, Combust. Sci. Technol. 22 (3–4) (1980) 143–169.
[22] V.V. Gubernov, V. Bykov, U. Maas, Hydrogen/air burner-stabilized flames at elevated pressures, Combust. Flame 185 (2017) 44–52.
[23] V.V. Bykov, V.V. Gubernov, U. Maas, Mechanisms performance and pressure dependence of hydrogen/air burner-stabilized flames, Math. Model. Nat. Phenom. 13 (6) (2018) 51.
[24] V Mislavskii, N Pestovskii, S Tskhai, B Kichatov, V.V. Gubernov, V Bykov, U Maas, Diffusive-thermal pulsations of burner stabilized methane-air flames, Combust. Flame 234 (2021) 111638.
[25] A Moroshkina, V Mislavskii, B Kichatov, V.V. Gubernov, V Bykov, U Maas, Burner stabilized flames: Towards reliable experiments and modelling of transient combustion, Fuel 332 (2023) 125754.
[26] Daniil Volkov, Anastasia Moroshkina, Vladimir Mislavskii, Evgeniy Sereshchenko, V.V Gubernov, Viatcheslav Bykov, Sergey Minaev, Relaxational oscillations of burner-stabilized premixed methane–air flames, Combust. Flame 259 (2024) 113141.
[27] AI Korsakova, VV Gubernov, AV Kolobov, V Bykov, U Maas, Stability of rich laminar hydrogen-air flames in a model with detailed transport and kinetic mechanisms, Combust. Flame 163 (2016) 478–486.
[28] A Moroshkina, E Yakupov, V Mislavskii, E Sereshchenko, A Polezhaev, S Minaev, V Gubernov, V Bykov, The performance of reaction mechanism in prediction of the characteristics of the diffusive-thermal oscillatory instability of methane–hydrogen–air burner-stabilized flames, Acta Astronaut. 215 (2024) 496–504.
[29] H. Jasak, Error analysis and estimation for finite volume method with applications to fluid flow (Ph.D. thesis), Imperial College (University of London), London SW7 2AZ, UK, 1996.
[30] T. Zirwes, F. Zhang, P. Habisreuther, M. Hansinger, H. Bockhorn, M. Pfitzner, D. Trimis, Quasi-DNS dataset of a piloted flame with inhomogeneous inlet conditions, Flow Turbul. Combust. 104 (4) (2020) 997–1027.
[31] T. Zirwes, M. Sontheimer, F. Zhang, A Abdelsamie, F.E.H. Pérez, O.T. Stein, H.G. Im, A. Kronenburg, H. Bockhorn, Assessment of numerical accuracy and parallel performance of OpenFOAM and its reacting flow extension EBIdnsFoam, Flow Turbul. Combust. 111 (2) (2023) 567–602.
[32] C.J. Greenshields, OpenFOAM user guide (version 7), CFD Direct Ltd. Tech. Rep. (2019).
[33] J.O. Hirschfelder, C.F. Curtiss, R.B. Bird, Molecular Theory of Gases and Liquids, John Wiley & Sons, 1964.
[34] Jurgen Warnatz, Ulrich Maas, Robert W. Dibble, J. Warnatz, Combustion, Springer, 2006.
[35] G.P. Smith, D.M. Golden, M. Frenklach, B. Eiteneer, Mikhail Goldenberg, C. Thomas Bowman, et al., GRI-mech 3.0, 2010, http://www.me.berkeley.ed/gri_mech/ (Accessed 14 March 2010).
[36] R.J. Hall, The radiative source term for plane-parallel layers of reacting combustion gases, J. Quant. Spectrosc. Radiat. Transfer 49 (5) (1993) 517–523.
[37] R.J. Hall, Radiative dissipation in planar gas-soot mixtures, J. Quant. Spectrosc. Radiat. Transfer 51 (4) (1994) 635–644.
[38] S.B. Margolis, Bifurcation phenomena in burner-stabilized premixed flames, Combust. Sci. Technol. 22 (3–4) (1980) 143–169.
[39] Kaoru Maruta, Takuya Kataoka, Nam Il Kim, Sergey Minaev, Roman Fursenko, Characteristics of combustion in a narrow channel with a temperature gradient, Proc. Combust. Inst. 30 (2005) 2429–2436.